Topological alloy engineering and locally linearized gap dependence on concentration

Dongwook Kim and Feng Liu*
Department of Materials Science and Engineering, University of Utah, Salt Lake City, Utah 84112, USA

(Received 30 March 2022; accepted 20 July 2022; published 4 August 2022)

Alloy engineering is a well-established approach to tune various materials' properties, but its application to topological alloys remains rudimentary. Of special interest is the band gap, the most defining property of topological materials; however, the concentration dependence of energy gaps in topological alloys remains unknown. Here we systematically investigate the band gap evolution of a topological alloy as a function of alloy concentration, using $KZnSb_{1-x}Bi_x$ as a prototype, based on first-principles calculations. In contrast to the well-established smooth bowing curve for a trivial gap in semiconductor alloys, we found that the topological gap evolves generally with a complex fragmented pattern due to topological phase transitions, and most strikingly a linear dependence on concentration locally in each distinct phase. Such gap linearization is fundamentally rooted in the linear dependence on alloy concentration of spin-orbit coupling (SOC) that predominantly determines a topological gap. Furthermore, we demonstrate topological alloy engineering as a general approach to tune the topological order by modulating the band edge composition and degeneracy through the alloying-induced interplay of SOC and atomic orbital on-site energy, while the linear gap dependence on alloy concentration remains independent of the degree of topological order.

DOI: 10.1103/PhysRevB.106.085105

I. INTRODUCTION

The band gap is one of the most fundamental physical quantities underlying the electrical, optical, and optoelectronic properties of crystalline materials with the Fermi level lying in an energy gap in the electronic band structure. For conventional semiconductors and insulators [1–3], electrical and photoelectrical conduction is highly correlated with the band gap size [4–13], as well as combination of gaps in heterojunctions [14,15]. Recently, a different type of "topologically gapped" insulator has been discovered, attracting much attention [16–26]. The topological gap, or the absence of it, not only signifies the topological order but also plays an important role in defining the strength of topological order, namely the energy window within which quantized surface/edge Hall conductivity resides and the transition temperature for a topological phase transition occurs.

Alloying is the one of the most effective methods used for tuning various materials' properties, such as mechanical, electrical, optoelectronic, and magnetic properties, which has been extensively studied in physics and materials community. In the simplest form, the effect of alloying is explained by Vegard's law [27,28], for which the property of an alloy, such as lattice constant, is linearly interpolated between those of the two pure phases while high-order terms are neglected. However, in terms of band gap of semiconductors, i.e., normal insulators in general, Vegard's law fails; instead, a well-known bowing curve is used to describe uniformly the dependence of band gap on alloy concentration over the whole composition range [4–12,29–37]. It indicates the general importance of nonlinear alloying effects, including (i) volume deformation, (ii) chemical electronegativity, and (iii) structural deformation [31,32,34,38].

Naturally, alloying has also been attempted to tune the properties of topological materials, such as to induce topological phase transitions [39–55]. However, most studies so far have been trial and error in nature focusing on a specific aspect related to alloying for a small composition variation. A general understanding of how topological gap depends on alloy concentration, especially over the whole composition range, is still lacking. This question is especially important because the topological alloys have usually a narrow gap which can be easily tuned by chemical composition, where not only the size but also the "sign" of gap can be changed because of band inversion. Furthermore, different from a charge gap in conventional semiconductors, which is determined by atomic orbital on-site energies and lattice hopping strength, a topological gap is critically determined by the strength of spin-orbit coupling (SOC), which is expected to have a different alloy concentration dependence with significant implications on topological alloying engineering. Here, we will answer this fundamental question by a systematic first-principles theoretical study, using $KZnSb_{1-x}Bi_x$ as a prototypical topological alloy.

II. CALCULATION METHODS

Our first-principles calculations are based on density functional theory (DFT) with plane-wave basis using QUANTUM ESPRESSO package [56] in the Perdew-Burke-Ernzerhof (PBE) type generalized gradient approximation (GGA) [57]. The norm-conserving nonlocal pseudopotentials are generated using OPIUM [58]. Alloying is considered within virtual crystal approximation (VCA), where an artificially "*A*-*B* alloyed"

*fliu@eng.utah.edu

atom is constructed by interpolating pseudopotentials of *A* and *B* atom, to represent a perfectly random distribution in the thermodynamic limit of an infinite alloy system. The energy cutoff for the basis is set to 50 Ry. The atomic structure is fully relaxed with the force threshold of $1e^{-2}$eV/Å, and the $9 \times 9 \times 9$ Monkhorst-Pack grid [59] is used for *k*-point sampling. The lattice constants of KZnSb (KZnBi) are calculated as $a = 4.52(4.69)$ Å and $c = 10.16(10.56)$ Å. The quasiparticle interference patterns (surface spectra) are obtained by calculating the surface Green's function for a semi-infinite geometry [60] by Wannier tools [61], with Wannier Hamiltonian generated using the WANNIER90 package [62]. In the Wannierization process, the (010) surface is constructed using a rectangular supercell consisting of two unit cells, with the conduction and valence states projected to the Zn *s* and Sb/Bi *p* orbitals near the Fermi level. We note that the VCA method can capture the alloying induced effects of volume deformation and chemical electronegativity but not structural deformation, which leads to an underestimation of bowing effect [38]. However, our objective is to obtain a general trend of TPTs and gap dependence on continuous change of concentration over the whole composition range (from 0 to 100%), for which the VCA method is a suitable and qualitatively reliable.

We discover a locally linearized dependence of topological gap on alloy concentration that is believed to be general to all topological alloys. First, instead of one smooth uniform bowing curve of gap evolution in semiconductors, topological alloys should usually exhibit multiple regions of different curves of gap evolution due to topological phase transitions, induced by gap closing and reopening processes accompanied with band inversion at given alloy concentrations. Second, within each region of a distinct topological phase, topological gap will "universally" evolve linearly with concentration. Apparently, in the region of a topological semimetal phase of zero gap, the gap "size" remains constant. Specifically, for $KZnSb_{1-x}Bi_x$, our first-principles calculations reveal a complex linear-constant-linear gap evolution curve with the increasing concentration, underlined by a sequential occurrence of three distinct phases of normal insulator (NI), Dirac semimetal (DSM) and topological crystalline insulator (TCI). It is revealed that this is caused by bands being inverted twice due to the alloying-induced interplay of SOC strength and on-site energy modulation. Furthermore, we demonstrate topological alloy engineering as a general approach to tune the topological order by modulating the band edge composition and degeneracy, while the linear gap dependence on alloy concentration is independent of the degree of topological order. We develop a tight-binding (TB) lattice model to explain and analyze the findings from first-principles calculations, using a nested Wilson loop method [see Fig. S1, Fig. S2, Table SI, and related discussions in the Supplemental Material (SM) [63]].

III. LOCALLY LINEARIZED GAP DEPENDENCE ON ALLOY CONCENTRATION

Both KZnSb and KZnBi crystals are the layer-structured *ABC* materials and belong to I-II-IV ternary compounds with an hcp structure [64–70], hosting various topological phases. Figure 1(a) shows the crystal structure of $KZnSb_{1-x}Bi_x$ alloy. As seen from the oblique view of the crystal structure [lower panel of Fig. 1(a)], the most stable structure has planar honeycomb layers composed of *B* site (Zn) and *C* site (Sb, Bi) atoms. It has space group no. 194 (*P*63/*mmc*), containing time reversal (T), inversion (P), and twofold (sixfold) rotation along the *x*-axis (*z*-axis) (C_{2x} and C_{6z}) symmetries. Figure 1(b) shows the bulk Brillouin zone (BZ) and the surface BZ projection of $KZnSb_{1-x}Bi_x$ alloys.

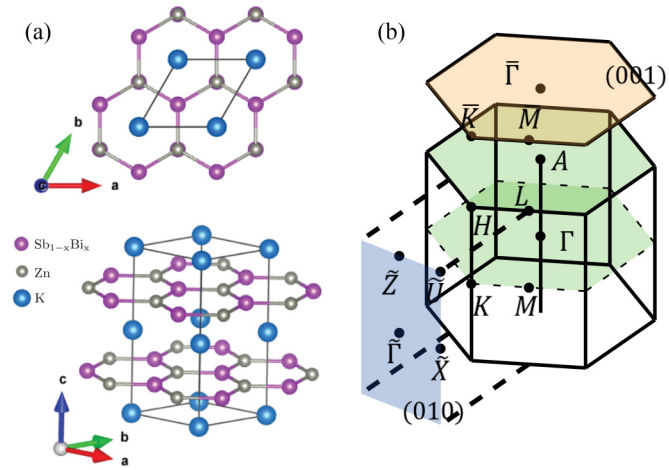

FIG. 1. Crystal structure and BZ of the $KZnSb_{1-x}Bi_x$ alloys. (a) Top view and oblique projection of crystal structure of $KZnSb_{1-x}Bi_x$ alloy. K, Zn, and Sb (Bi) atoms are represented by light blue, gray, and purple balls, respectively. (b) Bulk and surface Brillouin zone of $KZnSb_{1-x}Bi_x$ alloy.

Figure 2(a) shows the calculated band gap evolution curve of $KZnSb_{1-x}Bi_x$ over the whole composition range. One finds a gapless phase in between two gapped phases, which are identified to be NI, DSM, and hourglass TCI phases, respectively. In the range $x = 0.23$–0.45, the DSM phase is characterized with a pair of topological Dirac points (DPs). Such a complex evolution pattern of band gaps, consisting of four distinct regions, is attributed to two reasons: the double band inversion (DBI) and change of band edge representations of the conduction band minimum (CBM) and/or valence band maximum (VBM). From region I to II, a phase transition from NI to DSM occurs, triggered by a gap closing process. Within region II of DSM, there exist hidden gap opening and closing processes, accompanied by a change of band edge composition without changing band topology. From region II to III, a DSM to TCI phase transition occurs, triggered by a gap reopening process. Both regions III and IV are TCI phases but have a different gap dependence (slope) on alloy concentration, due to a change of valence band edge representation.

Interestingly, one notices that in each region of Fig. 2(a), the gap changes with alloy concentration linearly with negligible bowing effect. We argue that this predominantly originates from the fact that the SOC strength and hence the SOC gap has a linear dependence on alloy concentration. In other words, fundamentally a topological gap is predominantly determined by the SOC, different from a charge gap that is determined by on-site energies and lattice hopping strength. To confirm this, we plot the SOC splitting between the $j = 3/2$ and $j = 1/2$ states originating from the $Sb_{1-x}Bi_x$ *p* orbitals in Fig. 2(b),

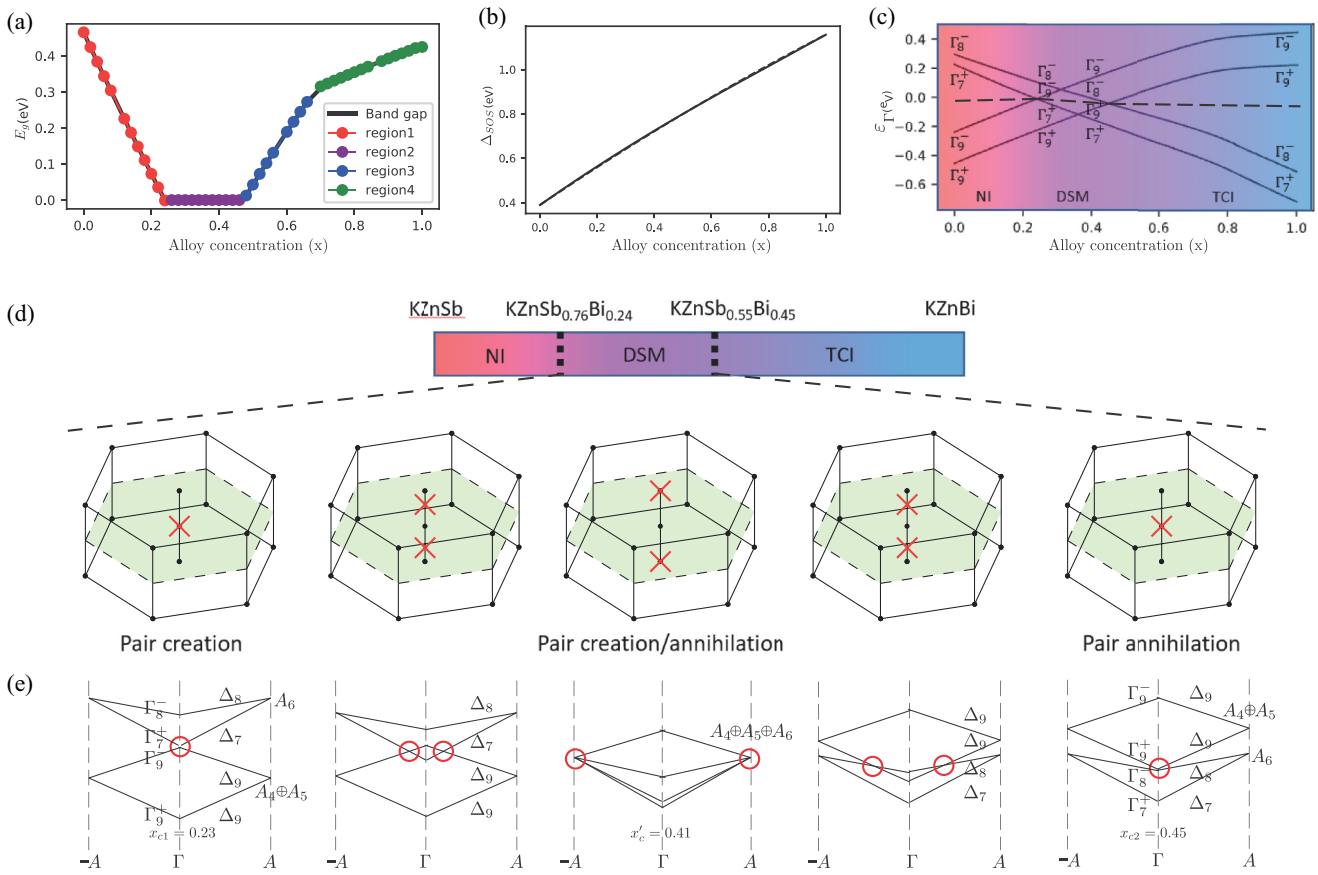

FIG. 2. Electronic structure evolution in $KZnSb_{1-x}Bi_x$ alloy. (a) Band gap (E_g) evolution of $KZnSb_{1-x}Bi_x$ alloy as a function of Bi alloy concentration ($\boldsymbol{x}$). (b) SOC splitting ($\boldsymbol{\Delta}_{\mathrm{SOC}}$) between $j = 3/2$ and $j = 1/2$ states at A point as a function of x. (c) Evolution of energy eigenvalue (ε_Γ) alignments and representations at Γ as a function of x. (d) Phase diagram as a function of x and schematic diagram of DP creation/annihilation during NI to TCI phase transition leading to DBI. Red cross marks the DP. (e) Schematic diagram of band crossings along high symmetric Γ-A line during DBI. DPs are highlighted by red circles.

reflecting the on-site SOC strength, which clearly shows a linear dependence on alloy concentration over the whole composition range $x = 0.0$–1.0. We note that the nonlinear effects, such as the one due possibly to structural deformation [32,38], are also suppressed by the existence of multiple phase transitions that divide the composition variation into smaller ranges within each topological phase, which makes the linear SOC term locally more dominant. Interestingly, if one looks globally at the gap curve over the whole composition range, it has actually a large bowing effect with the gap first decreasing and then increasing, as obtained from the VCA method, indicating that the gap linearization happens only locally within each segment of different phases.

IV. TOPOLOGICAL ALLOYING ENGINEERING

The discovered local linear gap dependence on alloy concentration provides a general and useful guideline to tune the topological phases by topological alloying engineering. Furthermore, we found that alloying will change the band edge composition (representation) and degeneracy by modulating the interplay between on-site SOC and atomic orbital energies, to induce not only topological phase transitions as mentioned above but also hidden high-order topological phases but without changing the linear gap dependence on concentration, as we illustrate below.

Overall, there are four regions of linear gap dependence with a different local slope. In region I, the band gap is direct and trivial in the presence of SOC that will nevertheless affect the trivial gap size; both CBM and VBM are located at the zone center with representation Γ_7^+ and Γ_9^-, respectively. In region II, there is a constant zero gap for a DSM phase. In regions III and IV, the gap is nontrivial and indirect. The CBM is always at Γ with representation Γ_9^+, but the VBM is at A with representation A_6 in region III and σ_5 in the middle of the high-symmetry $\Gamma - M$ line in region IV, respectively. This change of the VB edge is responsible for the change of slope of the band gap from region III to V, i.e., a kink in the band gap evolution curve at $x = 0.68$ within the TCI phase.

As mentioned above, there are DBIs during the NI-DSM-TCI phase transition over the whole composition range. This is because there are four bands instead of the usual two bands near the Fermi level that are involved with the topological phase transitions induced by alloying. Specifically, their representations at Γ are Γ_9^+, Γ_9^-, Γ_7^+, and Γ_8^-, respectively, and Fig. 2(c) shows the evolution of their relative alignments as a function of alloy concentration. The black dashed lines indicate the two critical alloy concentrations (x_{c1} and x_{c2})

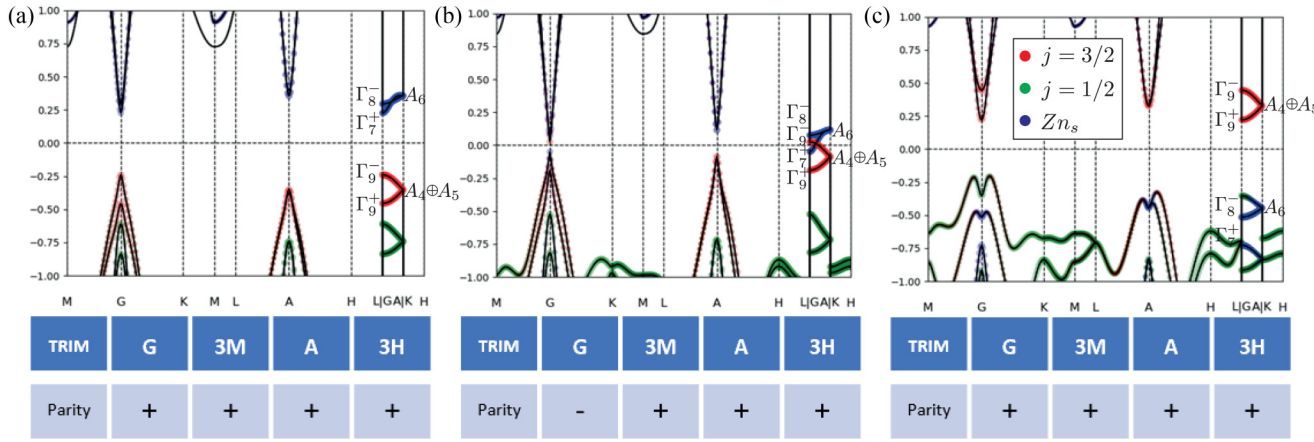

FIG. 3. Representative band structures illustrating band inversion in $KZnSb_{1-x}Bi_x$ alloy for three distinct phases [(a) NI, (b) DSM, and (c) TCI]. Atomic orbital projection of $j = 3/2$ and $j = 1/2$ are presented with red and blue colored dots, respectively (upper panel). Product of parity eigenvalues at TRIM for the occupied states (lower panel).

where the topological phase transitions occur. Therefore, there exist two phase transitions going from KZnSb to KZnBi by Bi alloying. The first NI-to-DSM transition occurs at $x_{c1} = 0.23$ by the inversion of Γ_9^+ and Γ_8^- states, while the second DSM-to-TCI phase transition occurs at $x_{c2} = 0.45$ by the inversion of Γ_7^+ and Γ_9^- states. Each band inversion indicates a topological transition. One can find a nontrivial Z_2 topology in the DSM phase confirmed by the odd times of inverted parity eigenvalues at time reversal invariant momenta (TRIM) [71]. On the other hand, the TCI phase is nontrivial with gapless boundary states protected by crystalline spatial symmetry (such as rotation symmetry discussed below), but has a trivial Z_2 topology defined by inversion symmetry. In other words, the TCI phase is made of two copies of Z_2 phases with bands inverted an even number of times.

The phase transition sequence of NI-DSM-TCI was modeled previously by the rotation symmetry analysis instead of alloying and explained by one sequence of creation and annihilation of DPs [72]. Interestingly, in $KZnSb_{1-x}Bi_x$, there exists a process of DBI, where the sequence of creation and annihilation of DPs happen twice due to alloying. To better understand the DBI, Fig. 2(d) shows the general phase diagram of $KZnSb_{1-x}Bi_x$ and a schematic diagram illustrating the behavior of DPs in the DSM phase, and Fig. 2(e) presents the schematic diagram of band structure evolution in terms of representations along the high symmetric line $A-\Gamma-A$. By compatibility relations, four states (Γ_9^+, Γ_9^-, Γ_7^+, and Γ_8^-) at Γ become Δ_9, Δ_9, Δ_7, and Δ_8 on the $\Gamma-A$ line. At the zone boundary, Δ_7 and Δ_8 merge into A_6 and two Δ_9 states merge into $A_4 \oplus A_5$.

The first NI-to-DSM phase transition is induced by the first band inversion that occurs at $x_{c1} = 0.23$ [first column of Figs. 2(d) and 2(e)], which is accompanied by the creation of a pair of DPs on the $\Gamma-A$ line. As the alloy concentration x increases, the separation of two DPs increases [second column of Figs. 2(d) and 2(e)]. At a "pseudocritical" alloy concentration $x_c' = 0.41$, the two DPs merge at the zone boundary A. This leads to an accidental band crossing, where the band degeneracy becomes eightfold, i.e., a doublet of DPs: $A_4(2) \oplus A_5(2) \oplus A_6(4)$. At the same time [third column of Figs. 2(d) and 2(e)], a new pair of DPs are created, but the system remains as a DSM with a different Fermi surface consisting of one eightfold DP doublet instead of two fourfold DP singlets. As x increases further [fourth column of Figs. 2(d) and 2(e)], two DPs reappear and move back toward the zone center. However, their representations change into Δ_8 and Δ_9 from the previous Δ_7 and Δ_9. Finally, the system reaches the second critical alloy concentration $x_{c2} = 0.45$ [last column of Figs. 2(d) and 2(e)], where a DP pair annihilation happens again but accompanied with gap opening, leading to the DSM-to-TCI phase transition.

Figure 3 shows the typical electronic band structures of three distinct phases at different alloy concentrations. The gapped band structures of pure KZnSb and KZnBi are shown in Figs. 3(a) and 3(c), respectively. In the alloy range $x = 0.23$–0.45, the alloy is gapless as for a DSM phase, whose band structure is represented in Fig. 3(b) using $x = 0.28$. In all cases, the most dominant atomic orbitals near the Fermi level are Zn s and Sb (Bi) p orbitals, which are common in this kind of ternary compounds [64,66,69]. The contribution from K in the intercalated site (the A site) is negligible. The energy difference of B-site s orbitals and C-site p orbitals, intertwined with SOC, plays an important role in defining the topological phases. With the increasing alloy concentration, the energy of the Zn-s and Sb/Bi-p dominated bands move downward and upward, respectively, causing eventually a gap closing and reopening process to induce topological phase transition.

The on-site energy and SOC strength at three selected alloy concentrations to represent NI, DSM, and TCI phases, respectively, are obtained by fitting a TB lattice model to DFT results, as tabulated in Table I (a table of all the pa-

TABLE I. Parameters of $KZnSb_{1-x}Bi_x$ lattice model (ε_s is for Zn atom, set to 0; ε_p is for Sb, Bi, or virtually alloyed atom of $Sb_{1-x}Bi_x$).

In unit of eV	KZnSb	$KZnSb_{0.72}Bi_{0.28}$	KZnBi
ε_s	0	0	0
$\varepsilon_{p_{x/y}}$	−6.728	−5.584	−4.509
ε_{p_z}	−4.528	−3.112	−2.163
λ_{SOC}	0.203	0.436	0.568

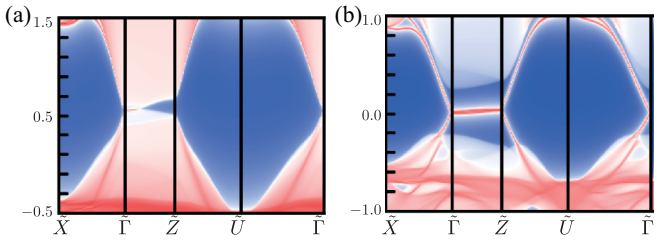

FIG. 4. Topological surface states of $KZnSb_{1-x}Bi_{x.28}$ illustrating the first-order topology in the DSM phase. (a) topological surface states of DSM phase ($x = 0.28$) on the (010) side surface, (b) topological surface states of TCI phase ($x = 1.0$) on the (010) side surface.

rameters for the TB model of alloy is available in the Table S1 in the SM [63]). As the concentration of Bi, which has a larger SOC, increases, the overall SOC strength increases. Also, it is the interplay between the changing on-site energies of Zn-s and $Sb_{1-x}Bi_x$-p orbitals and the changing SOC strength that determines the evolution of band topology. Specifically, in the range of Bi concentration between 0.23 and 0.45, the alloy is in the DSM phase, having a pair of DPs on the threefold rotational symmetry axis (k_x, $k_y = 0$: k_z axis). The electron and hole pockets are mainly composed of Zn s and Sb (Bi) p orbitals, respectively, and they touch at the DPs on the high symmetry line $\Gamma - A$. In one case shown in Fig. 3(b), this touching point is located at $0.153A$ $(0.0,\ 0.0,\ 0.153\frac{\pi}{c})$. Topological DPs exist as a pair in the BZ $[\pm 0.153A(0.0, 0.0, \pm 0.153\frac{\pi}{c})]$ due to the time reversal symmetry (TRS).

From the atomic projection, as represented by the color scheme in Fig. 3(b), one can see the trend of band inversion between the Zn s-originated $j = 1/2$ and Bi p-originated $j = 3/2$ bands, and the Z_2 topological invariant can be calculated by using the parity eigenvalues at TRIM [71]. The products of the parity eigenvalues at TRIM are presented in the lower panel of Fig. 3; their values at Γ show the inverted bands in the DSM phase and the twice inverted bands, i.e., DBI in the TCI phase, which have the nontrivial and trivial Z_2 topology, respectively. In the DSM phase, although the bands are inverted in the same way as in a TI, C_{3z} rotation symmetry protects the band degeneracy at the crossing point on the rotational axis (k_z axis), to prevent gap opening. Representations of the crossing bands are Δ_9 and Δ_8 in the little group C_{6v} on the high-symmetric $\Gamma - A$ line, which are both eigenstates of the C_{3z} rotational operator with eigenvalues of $e^{i\pi\sigma_z}$ and $e^{i(\pi/3)\sigma_z}$, respectively. Due to the compatibility relation, Δ_9 and Δ_8 evolve into Γ_9^+ and Γ_8^- at Γ, respectively.

Figure 4 shows the topological surface states in the DSM and TCI phases. In the DSM phase, the $k_z = 0$ and $k_z = \pi$ plane have different Z_2 numbers computed by using the Fu-Kane formula [71] or Wilson loop calculation [73] due to the band inversion at Γ. We have calculated the quasiparticle interference (QPI) spectra by using the surface Green's function method [60]. In the DSM phase [Fig. 4(a)], there are an odd number of surface states between the two projected DPs on the $\tilde{\Gamma} - \tilde{Z}$ line of the (010) surface BZ. On the other hand, in the TCI phase [Fig. 4(b)], the well-known hourglass surface states can be found inside the bulk band gap.

Moreover, the topological DP can be a singular point for a higher-order topological phase transition [74]. Indeed, in the DSM phase, we found there exists nontrivial higher-order topology, based on the nested Wilson loop calculation [74–76] [see Fig. S2(m) in the SM [63]], using the lattice TB model of the DSM phase with the parameters listed in Table SI in the SM [63]. The nontrivial winding in the nested Wilson loop calculation with 1/3 or 2/3 Wilson bands on every k_z slice indicates nontrivial second-order phase transition across the DPs subject to the C_{3z} symmetry [see Figs. S1(e) and S1(h) in the SM [63]]. It means that breaking the C_{3z} symmetry would open a gap at the two DPs on the k_z line, which trivializes the second-order topology but preserves the first-order topology by turning the DSM phase into a TI phase (see Fig. S2 in the SM [63]).

V. CONCLUSION

We reveal a locally linearized gap dependence on concentration in $KZnSb_{1-x}Bi_x$, which is believed to be general to all topological alloys. Because not only the size but also the sign of topological gap will change with varying alloy concentration, generally the topological gap exhibits a fragmented gap evolution with concentration, rather than a uniform evolution for a trivial gap, such as the well-known bowing curve for a semiconducting gap. Most strikingly, within each fragment the topological gap, predominantly determined by SOC, changes linearly with concentration. Specifically, for $KZnSb_{1-x}Bi_x$, there exist double band inversions leading to a sequence of NI-DSM-TCI phase transitions. The DSM phase is also found with second-order topology due to the alloying induced interplay between on-site energy and SOC. Our findings provide a general understanding of the topologically gapped alloys and a useful guideline to manipulate and control topological phases by alloy engineering.

ACKNOWLEDGMENTS

This work was supported by U.S. DOE-BES (Grant No. DE-FG02-04ER46148). Support from the CHPC at the University of Utah and the NERSC at the Office of Science of the U.S. Department of Energy is gratefully acknowledged.

[1] B. G. Yacobi, *Semiconductor Materials: An Introduction to Basic Principles* (Springer, New York, 2003).

[2] M. Fox, *Optical Properties of Solids* (Oxford University Press, Oxford, 2010).

[3] Z. C. Feng, *III-Nitride Semiconductor Materials* (World Scientific, Singapore, 2006).

[4] S.-H. Wei and A. Zunger, Giant and Composition-Dependent Optical Bowing Coefficient in Gaasn Alloys, Phys. Rev. Lett. **76**, 664 (1996).

[5] H. J. Conley, B. Wang, J. I. Ziegler, R. F. Haglund, S. T. Pantelides, and K. I. Bolotin, Bandgap engineering of strained monolayer and bilayer MoS_2, Nano Lett. **13**, 3626 (2013).

[6] H. Li, X. Duan, X. Wu, X. Zhuang, H. Zhou, Q. Zhang, X. Zhu, W. Hu, P. Ren, P. Guo *et al.*, Growth of alloy $MoS_{2x}Se_{2(1-x)}$ nanosheets with fully tunable chemical compositions and optical properties, J. Am. Chem. Soc. **136**, 3756 (2014).

[7] S. Tongay, D. S. Narang, J. Kang, W. Fan, C. Ko, A. V. Luce, K. X. Wang, J. Suh, K. D. Patel, V. M. Pathak *et al.*, Two-Dimensional semiconductor Alloys: monolayer $MoS_{2x}Se_{2(1-x)}$, Appl. Phys. Lett. **104**, 012101 (2014).

[8] M. Zhang, J. Wu, Y. Zhu, D. O. Dumcenco, J. Hong, N. Mao, S. Deng, Y. Chen, Y. Yang, C. Jin *et al.*, Two-Dimensional molybdenum tungsten diselenide Alloys: Photoluminescence, raman Scattering, and electrical transport, ACS Nano **8**, 7130 (2014).

[9] Y. Chen, J. Xi, D. O. Dumcenco, Z. Liu, K. Suenaga, D. Wang, Z. Shuai, Y.-S. Huang, and L. Xie, Tunable band gap photoluminescence from atomically thin transition-metal dichalcogenide alloys, ACS Nano **7**, 4610 (2013).

[10] J. A. Van Vechten and T. K. Bergstresser, Electronic structures of semiconductor alloys, Phys. Rev. B **1**, 3351 (1970).

[11] D. Richardson and R. Hill, The origins of energy gap bowings in substitutional semiconductor alloys, J. Phys. C Solid State Phys. **5**, 821 (1972).

[12] A. Zunger and J. E. Jaffe, Structural Origin of Optical Bowing in Semiconductor Alloys, Phys. Rev. Lett. **51**, 662 (1983).

[13] Q. Yan, B. Huang, J. Yu, F. Zheng, J. Zang, J. Wu, B.-L. Gu, F. Liu, and W. Duan, Intrinsic current−voltage characteristics of graphene nanoribbon transistors and effect of edge doping, Nano Lett. **7**, 1469 (2007).

[14] B. Huang, M. Yoon, B. G. Sumpter, S.-H. Wei, and F. Liu, Alloy Engineering of Defect Properties in Semiconductors: Suppression of Deep Levels in Transition-Metal Dichalcogenides, Phys. Rev. Lett. **115**, 126806 (2015).

[15] Z. Liu, J. Wu, W. Duan, M. G. Lagally, and F. Liu, Electronic Phase Diagram of Single-Element Silicon "Strain" Superlattices, Phys. Rev. Lett. **105**, 016802 (2010).

[16] W. Jiang, X. Ni, and F. Liu, Exotic topological bands and quantum states in metal–organic and covalent–organic frameworks, Acc. Chem. Res. **54**, 416 (2021).

[17] M. Z. Hasan and J. E. Moore, Three-Dimensional topological insulators, Annu. Rev. Condens. Matter Phys. **2**, 55 (2011).

[18] S. Rachel, Interacting topological Insulators: a review, Rep. Prog. Phys. **81**, 116501 (2018).

[19] Y. Tokura, K. Yasuda, and A. Tsukazaki, Magnetic topological insulators, Nat. Rev. Phys. **1**, 126 (2019).

[20] M. Z. Hasan and C. L. Kane, Colloquium: topological insulators, Rev. Mod. Phys. **82**, 3045 (2010).

[21] X.-L. Qi and S.-C. Zhang, Topological insulators and superconductors, Rev. Mod. Phys. **83**, 1057 (2011).

[22] M. Franz and L. Molenkamp, *Topological Insulators* (Elsevier, Oxford, 2013).

[23] F. Ortmann, S. Roche, S. O. Valenzuela, and L. W. Molenkamp, *Topological Insulators: Fundamentals and Perspectives* (Wiley, Berlin, 2015).

[24] B. A. Bernevig and T. L. Hughes, *Topological Insulators and Topological Superconductors, STU-Student edition* (Princeton University Press, Princeton, 2013).

[25] D. E. Cohen, *Combinatorial Group Theory: A Topological Approach,* Vol. 14 (Cambridge University Press, Cambridge, UK, 1989).

[26] S.-Q. Shen, *Topological Insulators: Dirac Equation in Condensed Matter, Vol. 187* (Springer, Singapore, 2017).

[27] A. R. Denton and N. W. Ashcroft, Vegard's law, Phys. Rev. A **43**, 3161 (1991).

[28] L. Vegard, Die konstitution der mischkristalle und die raumfüllung der atome, Z. Phys. **5**, 17 (1921).

[29] J. Wu, W. Walukiewicz, K. M. Yu, J. W. Ager, S. X. Li, E. E. Haller, H. Lu, and W. J. Schaff, Universal bandgap bowing in Group-III nitride alloys, Solid State Commun. **127**, 411 (2003).

[30] J. Wu, W. Walukiewicz, K. M. Yu, J. W. Ager, III, E. E. Haller, I. Miotkowski, A. K. Ramdas, C.-H. Su, I. K. Sou, R. C. C. Perera, and J. D. Denlinger, Origin of the large band-gap bowing in highly mismatched semiconductor alloys, Phys. Rev. B **67**, 035207 (2003).

[31] N. Tit, I. M. Obaidat, and H. Alawadhi, Origins of bandgap bowing in compound-semiconductor common-cation ternary alloys, J. Phys. Cond. Matter **21**, 075802 (2009).

[32] C. S. Schnohr, Compound semiconductor Alloys: from atomic-scale structure to bandgap bowing, Appl. Phys. Rev. **2**, 031304 (2015).

[33] H.-L. Shi and Y. Duan, Band-Gap bowing and p-Type doping of (Zn, Mg, Be)O wide-gapsemiconductor Alloys: a first-principles study, Eur. Phys. J. B **66**, 439 (2008).

[34] M. Ferhat, Computational optical band gap bowing of III–V semiconductors alloys, Phys. Status Solidi B **241**, R38 (2004).

[35] Y. Nabetani, T. Mukawa, Y. Ito, T. Kato, and T. Matsumoto, Epitaxial growth and large band-gap bowing of ZnSeO alloy, Appl. Phys. Lett. **83**, 1148 (2003).

[36] S.-H. Wei and A. Zunger, Band-gap narrowing in ordered and disordered semiconductor alloys, Appl. Phys. Lett. **56**, 662 (1990).

[37] W. G. Bi and C. W. Tu, N incorporation in GaP and band gap bowing of GaN_xP_{1-x}, Appl. Phys. Lett. **69**, 3710 (1996).

[38] J. E. Bernard and A. Zunger, Electronic structure of ZnS, ZnSe, ZnTe, and their pseudobinary alloys, Phys. Rev. B **36**, 3199 (1987).

[39] H. Huang, K.-H. Jin, and F. Liu, Alloy Engineering of Topological Semimetal Phase Transition in $MgTa_{2-x}Nb_xN_3$, Phys. Rev. Lett. **120**, 136403 (2018).

[40] X. Zhang, B. Cui, M. Zhao, and F. Liu, Topological states in a two-dimensional metal alloy in si Surface: BiAg/Si(111) − 4×4 surface, Phys. Rev. B **97**, 085422 (2018).

[41] L. B. Abdalla, E. P. José, T. M. Schmidt, R. H. Miwa, and A. Fazzio, Topological phase transitions of $(Bi_xSb_{1-x})_2Se_3$ alloys by density functional theory, J. Phys.: Condens. Matter **27**, 255501 (2015).

[42] H.-X. Deng, Z.-G. Song, S.-S. Li, S.-H. Wei, and J.-W. Luo, Atomic-Ordering-Induced quantum phase transition between topological crystalline insulator and Z_2 topological insulator, Chin. Phys. Lett. **35**, 057301 (2018).

[43] P. Dziawa, B. J. Kowalski, K. Dybko, R. Buczko, A. Szczerbakow, M. Szot, E. Łusakowska, T. Balasubramanian, B. M. Wojek, M. H. Berntsen *et al.*, Topological crystalline insulator states in $Pb_{1-x}Sn_xSe$, Nat. Mater. **11**, 1023 (2012).

[44] H. Guo, K. Sugawara, A. Takayama, S. Souma, T. Sato, N. Satoh, A. Ohnishi, M. Kitaura, M. Sasaki, Q.-K. Xue, and T. Takahashi, Evolution of surface states in $Bi_{1-x}Sb_x$ alloys across the topological phase transition, Phys. Rev. B **83**, 201104(R) (2011).

[45] G. Krizman, B. A. Assaf, T. Phuphachong, G. Bauer, G. Springholz, L. A. de Vaulchier, and Y. Guldner, Dirac parameters and topological phase diagram of $Pb_{1-x}Sn_xSe$ from magnetospectroscopy, Phys. Rev. B **98**, 245202 (2018).

[46] J. Liu and D. Vanderbilt, Topological phase transitions in $(Bi_{1-x}In_x)_2Se_3$ and $(Bi_{1-x}Sb_x)_2Se_3$, Phys. Rev. B **88**, 224202 (2013).

[47] H. Lu, X. Zhang, Y. Bian, and S. Jia, Topological phase transition in single crystals of $(Cd_{1-x}Zn_x)_3As_2$, Sci. Rep. **7**, 3148 (2017).

[48] P. S. Mandal, G. Springholz, V. V. Volobuev, O. Caha, A. Varykhalov, E. Golias, G. Bauer, O. Rader, and J. Sánchez-Barriga, Topological quantum phase transition from mirror to time reversal symmetry protected topological insulator, Nat. Commun. **8**, 968 (2017).

[49] A. Narayan, D. Di Sante, S. Picozzi, and S. Sanvito, Topological Tuning in Three-Dimensional Dirac Semimetals, Phys. Rev. Lett. **113**, 256403 (2014).

[50] C. Niu, P. M. Buhl, G. Bihlmayer, D. Wortmann, S. Blügel, and Y. Mokrousov, Two-Dimensional topological crystalline insulator and topological phase transition in TlSe and TlS monolayers, Nano Lett. **15**, 6071 (2015).

[51] B. Singh, A. Sharma, H. Lin, M. Z. Hasan, R. Prasad, and A. Bansil, Topological electronic structure and weyl semimetal in the $TlBiSe_2$ class of semiconductors, Phys. Rev. B **86**, 115208 (2012).

[52] S.-Y. Xu, C. Liu, N. Alidoust, M. Neupane, D. Qian, I. Belopolski, J. D. Denlinger, Y. J. Wang, H. Lin, L. A. Wray *et al.*, Observation of a topological crystalline insulator phase and topological phase transition in $Pb_{1-x}Sn_xTe$, Nat. Commun. **3**, 1192 (2012).

[53] C.-L. Zhang, T. Liang, N. Ogawa, Y. Kaneko, M. Kriener, T. Nakajima, Y. Taguchi, and Y. Tokura, Highly tunable topological system based on PbTe-SnTe binary alloy, Phys. Rev. Materials **4**, 091201(R) (2020).

[54] W. Zhang, R. Yu, H.-J. Zhang, X. Dai, and Z. Fang, First-Principles studies of the three-dimensional strong topological insulators Bi_2Te_3, Bi_2Se_3 and Sb_2Te_3, New J. Phys. **12**, 065013 (2010).

[55] T. Zhou, M. Tong, Y. Zhang, X. Xie, Z.-Y. Wang, T. Jiang, X.-G. Zhu, and X.-C. Lai, Topological phase transition in Sb-Doped Mg_3Bi_2 monocrystalline thin films, Phys. Rev. B **103**, 125405 (2021).

[56] P. Giannozzi, S. Baroni, N. Bonini, M. Calandra, R. Car, C. Cavazzoni, D. Ceresoli, G. L. Chiarotti, M. Cococcioni, I. Dabo *et al.*, QUANTUM ESPRESSO: A modular and open-source software project for quantum simulations of materials, J. Phys. Cond. Matter **21**, 395502 (2009).

[57] J. P. Perdew, K. Burke, and M. Ernzerhof, Generalized Gradient Approximation Made Simple, Phys. Rev. Lett. **77**, 3865 (1996).

[58] A. M. Rappe, K. M. Rabe, E. Kaxiras, and J. D. Joannopoulos, Optimized pseudopotentials, Phys. Rev. B **41**, 1227 (1990).

[59] H. J. J. Monkhorst and J. D. D. Pack, Special points for brillouin-zone integrations, Phys. Rev. B **13**, 5188 (1976).

[60] M. P. L. Sancho, J. M. L. Sancho, J. M. L. Sancho, and J. Rubio, Highly convergent schemes for the calculation of bulk and surface green functions, J. Physics F Metal Phys. **15**, 851 (1985).

[61] Q. Wu, S. Zhang, H.-F. Song, M. Troyer, and A. A. Soluyanov, WannierTools: An open-source software package for novel topological materials, Comput. Phys. Commun. **224**, 405 (2018).

[62] N. Marzari, A. A. Mostofi, J. R. Yates, I. Souza, and D. Vanderbilt, Maximally localized wannier Functions: theory and applications, Rev. Mod. Phys. **84**, 1419 (2012).

[63] See Supplemental Material at http://link.aps.org/supplemental/10.1103/PhysRevB.106.085105 for topological alloy engineering and locally linearized gap dependence on concentration.

[64] A. Parveen, E. Narsimha Rao, B. Adivaiah, P. Anees, and G. Vaitheeswaran, Topological behaviour of ternary non-symmorphic crystals KZ_nX (X = P, As, Sb) under pressure and Strain: a first principles study, Phys. Chem. Chem. Phys. **20**, 5084 (2018).

[65] C.-S. Kuo, T.-R. Chang, S.-Y. Xu, and H.-T. Jeng, Unconventional topological phase transition in non-symmorphic material KH_gX (X = As, Sb, Bi), npj Comput. Mater. **5**, 65 (2019).

[66] H.-J. Zhang, S. Chadov, L. Müchler, B. Yan, X.-L. Qi, J. Kübler, S.-C. Zhang, and C. Felser, Topological Insulators in Ternary Compounds with a Honeycomb Lattice, Phys. Rev. Lett. **106**, 156402 (2011).

[67] Z. Wang, A. Alexandradinata, R. J. Cava, and B. A. Bernevig, Hourglass fermions, Nature (London) **532**, 189 (2016).

[68] J. Ma, C. Yi, B. Lv, Z. Wang, S. Nie, L. Wang, L. Kong, Y. Huang, P. Richard, P. Zhang *et al.*, Experimental evidence of hourglass fermion in the candidate nonsymmorphic topological insulator KH_gSb, Sci. Adv. **3**, e1602415 (2017).

[69] X. Zhang, Q. Liu, Q. Xu, X. Dai, and A. Zunger, Topological insulators versus topological dirac semimetals in honeycomb compounds, J. Am. Chem. Soc. **140**, 13687 (2018).

[70] A. Alexandradinata, Z. Wang, and B. A. Bernevig, Topological Insulators from Group Cohomology, Phys. Rev. X **6**, 021008 (2016).

[71] L. Fu and C. L. Kane, Topological insulators with inversion symmetry, Phys. Rev. B **76**, 045302 (2007).

[72] B.-J. Yang and N. Nagaosa, Classification of stable three-dimensional dirac semimetals with nontrivial topology, Nat. Commun. **5**, 4898 (2014).

[73] A. Alexandradinata, X. Dai, and B. A. Bernevig, Wilson-Loop characterization of inversion-symmetric topological insulators, Phys. Rev. B **89**, 155114 (2014).

[74] B. J. Wieder, Z. Wang, J. Cano, X. Dai, L. M. Schoop, B. Bradlyn, and B. A. Bernevig, Strong and fragile topological dirac semimetals with higher-order fermi arcs, Nat. Commun. **11**, 627 (2020).

[75] W. A. Benalcazar, B. A. Bernevig, and T. L. Hughes, Electric multipole Moments, topological multipole moment Pumping, and chiral hinge states in crystalline insulators, Phys. Rev. B **96**, 245115 (2017).

[76] F. Schindler, A. M. Cook, M. G. Vergniory, Z. Wang, S. S. P. Parkin, B. A. Bernevig, and T. Neupert, Higher-Order topological insulators, Sci. Adv. **4**, eaat0346 (2018).